

Quantum simulation of spin-boson models with structured bath

Received: 30 November 2024

Accepted: 14 April 2025

Published online: 30 April 2025

Ke Sun ^{1,2,6}, Mingyu Kang ^{1,2,6}, Hanggai Nuomin ³, George Schwartz^{1,2}, David N. Beratan ^{2,3,4}, Kenneth R. Brown ^{1,2,3,5} & Jungsang Kim ^{1,2,5} ✉

The spin-boson model, involving spins interacting with a bath of quantum harmonic oscillators, is a widely used representation of open quantum systems that describe many dissipative processes in physical, chemical and biological systems. Trapped ions present an ideal platform for simulating the quantum dynamics of such models, by accessing both the high-quality internal qubit states and the motional modes of the ions for spins and bosons, respectively. We demonstrate a fully programmable method to simulate dissipative dynamics of spin-boson models using a chain of trapped ions, where the initial temperature and the spectral densities of the boson bath are engineered by controlling the state of the motional modes and their coupling with qubit states. Our method provides a versatile and precise experimental tool for studying open quantum systems.

Interaction of a quantum system with its environment in an open dissipative setting can significantly influence its dynamics. A paradigmatic model of non-Markovian open quantum systems that captures the quantum nature of both the system and the environment is the spin-boson model¹, which is ubiquitous in the study of condensed-matter physics^{2,3}, chemical reactions^{4,5}, collective modes in atomic-photon systems^{6,7}, and biological light-harvesting complexes^{8,9}. Experimentally realizing the dynamics of spin-boson models in a programmable fashion is an exciting challenge^{10–13}, which can lead to new quantum simulation approaches that reach beyond classically tractable limit.

Trapped ions provide a highly controllable system of spins and bosonic motional modes, and thus are a natural platform for simulating spin-boson models. The bosonic bath can be simulated using either a large number (≥ 50) of motional modes¹⁴ or a handful of dissipative motional modes^{15–18}. While significant experimental progress has been made in controlling the qubits and motional modes together^{19–21}, past works in this direction were limited to simulating a spin coherently coupled to up to two bosonic modes^{22–25}. These studies could not consider the effects of dissipation often described by coupling of the system to a continuum of bath modes, which determines the system's long-term behavior such as reaching a steady state. A simulation study

of a spin dissipatively coupled to several modes was reported recently, albeit with limited tunability²⁶.

Dissipative couplings come in two flavors: *damping* is when the quantum system exchanges energy with the bath (inelastic coupling) and eventually reaches thermal equilibrium with the bath, while *dephasing* is when the phase of the quantum system is randomized by interaction with the bath without energy exchange (elastic coupling). In this work, we perform quantum simulations of spin-boson models with programmable spectral densities using a 7-ion chain and up to 3 of its motional modes. The target spectral densities of the bath are decomposed into several Lorentzian peaks, which is characteristic of baths in real-world systems such as light-harvesting protein complexes^{27,28}. Our approach can readily simulate the dephasing model of dissipation, by adding randomness to the control parameters of the laser that drives the spin-boson interaction, such as frequency and phase. Using this technique, we study the dynamics of typical spin-boson models¹ and the vibration-assisted energy transfer (VAET) process²⁴.

Our demonstrated ability to engineer spectral density of the bath in analog quantum simulations is an important ingredient for achieving quantum advantage in studying open quantum system models that are intractable using classical methods^{17,18}.

¹Duke Quantum Center, Duke University, Durham, NC, USA. ²Department of Physics, Duke University, Durham, NC, USA. ³Department of Chemistry, Duke University, Durham, NC, USA. ⁴Department of Biochemistry, Duke University, Durham, NC, USA. ⁵Department of Electrical and Computer Engineering, Duke University, Durham, NC, USA. ⁶These authors contributed equally: Ke Sun, Mingyu Kang. ✉e-mail: jungsang@duke.edu

Results

Dephased spin-oscillator model

The spin-boson model describes a spin coupled to a continuous bath of quantum harmonic oscillators. The Hamiltonian is given by

$$\hat{H} = \hat{H}_S + \hat{H}_B + \frac{\hat{\sigma}_Z}{2} \otimes \int_0^\infty d\omega \sqrt{\frac{J(\omega)}{\pi}} (\hat{a}(\omega) + \hat{a}^\dagger(\omega)), \quad (1)$$

where $J(\omega)$ is the spectral density of the bath, $\hat{a}(\omega)$ is the annihilation operator of the bath oscillator at frequency ω , and $\hat{H}_S = \frac{\epsilon}{2} \hat{\sigma}_Z + \frac{\Delta}{2} \hat{\sigma}_X$ and $\hat{H}_B = \int_0^\infty d\omega \hat{a}^\dagger(\omega) \hat{a}(\omega)$ are the Hamiltonian of the spin and the bath, respectively. Here, ϵ and Δ are the detuning and coupling strength between the spin states, respectively, and \hbar is set to 1 for simplicity. We assume that the spin is initially in the $|0\rangle$ state (or the “donor” state in the energy transfer model) and the time evolution of the Hamiltonian induces population transfer to the $|1\rangle$ state (or the “acceptor” state). Each bath oscillator of frequency ω is in the thermal state of average phonon number $\bar{n}(\omega) = 1/(e^{\beta\omega} - 1)$, where β is the inverse of the temperature ($k_B = 1$ for simplicity).

We decompose the spectral density $J(\omega)$ of a structured bath into a sum of multiple Lorentzian peaks, each of which can be represented by a dissipative harmonic oscillator¹⁵. In this work, we consider a spin coupled to several oscillators subject to constant dephasing (“dephased” spin-oscillator model). This discrete oscillator model is described by the Hamiltonian

$$\hat{H}_D = \hat{H}_S + \sum_l \frac{\kappa_l}{2} \hat{\sigma}_Z \otimes (\hat{b}_l + \hat{b}_l^\dagger) + \sum_l \nu_l \hat{b}_l^\dagger \hat{b}_l \quad (2)$$

and corresponding Lindblad operators $\hat{L}_l = \sqrt{\Gamma_l} \hat{b}_l^\dagger \hat{b}_l$, where κ_l represents the coupling strength between the spin and l -th oscillator, ν_l and Γ_l denote the frequency and the dephasing rate of the l -th oscillator, respectively, and \hat{b}_l is the annihilation operator of the l -th oscillator. The composite state ρ of spin and oscillators follows the Lindblad master equation $\dot{\rho} = -i[\hat{H}_D, \rho] + \sum_l (\hat{L}_l \rho \hat{L}_l^\dagger - \frac{1}{2} \{\hat{L}_l^\dagger \hat{L}_l, \rho\})$. In a reasonable regime of parameters ($\Gamma_l < \nu_l/2, \beta \ll 2\pi(\Gamma_l/2)^{-1}$)¹⁵, this bath of dephased oscillators is assigned a spectral density composed of Lorentzian peaks

$$J_{l0}(\omega) = \sum_l \kappa_l^2 \left(\frac{\Gamma_l/2}{(\Gamma_l/2)^2 + (\omega - \nu_l)^2} - \frac{\Gamma_l/2}{(\Gamma_l/2)^2 + (\omega + \nu_l)^2} \right), \quad (3)$$

where we assume that each oscillator is initially in the thermal state with average phonon number $\bar{n}(\nu_l)$.

The spectral density of the bath determines the dynamics of the spin to leading order in $\bar{\kappa}T$, where $\bar{\kappa}$ is the average coupling strength and T is the evolution time (see Section III of the Supplementary Material). Therefore, the spin dynamics of the dephased spin-oscillator model approximately match those of the spin-boson model with $J(\omega) = J_{l0}(\omega)$ in the weak- $\bar{\kappa}$ regime. In the unbiased ($\epsilon = 0$) spin-boson model^{1,29–31}, the equilibrium donor-state population is 1/2 for both models, and we expect the population dynamics of the two models show an excellent match at all times for weak spin-bath coupling (Supplementary Fig. 4). For the case of biased spin-boson models in the stronger coupling regime ($\epsilon \neq 0$, such as discussed in the VAET case), the dynamics of the dephased spin-oscillator model we simulate can deviate significantly from the traditional spin-boson model.

A more common model for dissipation is a spin coupled to oscillators subject to constant damping (“damped” spin-oscillator model) described by a pair of Lindblad operators $\hat{L}_{l1} = \sqrt{\Gamma_l(\bar{n}(\nu_l) + 1)} \hat{b}_l$ and $\hat{L}_{l2} = \sqrt{\Gamma_l \bar{n}(\nu_l)} \hat{b}_l^\dagger$ ^{15,16}, where Γ_l here is the damping rate of the l -th oscillator. A stronger result holds for this model: the spin dynamics are non-perturbatively equivalent to those of the spin-boson model with the same spectral density, up to all orders in $\bar{\kappa}T$ ³². Damped oscillators

can be realized in trapped ions using sympathetic cooling on a chain of ions with multiple atomic species or isotopes^{15,16}, or using qubits encoded in different internal-state manifolds of the same type of ions³³. In fact, a recent work reported simulation of electron-transfer model using sympathetic cooling on the motional mode of a trapped ion³⁴. The dephased oscillator model developed in this work expands the ability to simulate a broader set of bath models not experimentally accessible before.

Experimental implementation

The simulations of spin-boson models are performed using a linear chain of seven ¹⁷¹Yb⁺ ions (Fig. 1). Two hyperfine internal states ($|0\rangle$ and $|1\rangle$) are used to represent the spin (or qubit). The ions sit 68 μm above the surface of the trap³⁵, and the heating rate and decoherence time of the zig-zag motional mode are 3.6(3) quanta/s and 5.2(7) ms, respectively. The other motional modes used have similar magnitudes. Details of our experimental setup can be found in Ref. 36. Using Doppler, electromagnetically-induced transparency (EIT), and sideband cooling techniques, the zig-zag motional mode can be cooled to near ground state with $\bar{n} = 0.036(16)$. Standard qubit manipulation techniques can be used to initialize and measure the qubits, and single-qubit operations are driven by stimulated Raman transitions. The spin-oscillator coupling is simulated using the spin-dependent kick (SDK) operation induced by simultaneous application of blue- and red-sideband transitions (see Methods).

The evolution of \hat{H}_D in Eq. (2) is mapped to a sequence of single-qubit rotations and SDK operations via Trotterization. We apply time evolution operators over a short time interval corresponding to each term in the Hamiltonian in the interaction picture, and repeat them over many time intervals to simulate the evolution dynamics (see Methods). This approach can be readily extended to simulating more complicated molecular models consisting of many electronic states and bath modes^{18,37}.

The dephased spin-oscillator model can be simulated using trapped ions by applying the SDK operations, which induce the coupling between the qubit and the motional mode. By adding randomness to the control parameters of the SDK operations and averaging the results over many random trials, we can implement dissipative processes such as preparing the thermal state and simulating the dephasing of the motional mode. The key idea is that certain dissipative evolutions described by the Lindblad master equation are equivalent to an average of many coherent evolutions, each subject to a stochastic Hamiltonian³⁸. Details of the procedure is described in Methods.

Single-oscillator case

We first consider a single-oscillator case ($l = 1$), and demonstrate the programmability of the bath’s initial temperature quantified by the oscillator’s average phonon number \bar{n} . Controlled amounts of resonant SDK operations with stochastically varying phase are applied to the ion prepared near the motional ground state, which prepares the thermal state equivalent to an ensemble of randomly displaced coherent states (see Methods). Figure 2a illustrates the simulated time evolution of the donor state population when it is coupled to such initial bath state, for various values of \bar{n} . The dynamics exhibit coherent oscillations with an envelope of slow collapse and revival (beat-note) that signifies resonant ($\nu_1 = \Delta$) energy exchange between the system and the bath oscillator³⁹. A thermal state of larger \bar{n} is a mixture of wider range of coherent states, leading to reduced beat-note amplitude at $t \approx 2\pi/\Delta \times 10.5$.

We compare our experimental results with the predictions of “noise-aware” models, reflecting inherent noise processes in the experimental setup. We fit the experimental data using an oscillator model with initial phonon number $\bar{n} + \bar{n}_0$ and Lorentzian spectral density with full width at half maximum (FWHM) $\Gamma_1 \equiv \Gamma$ [Eq. (3)], where

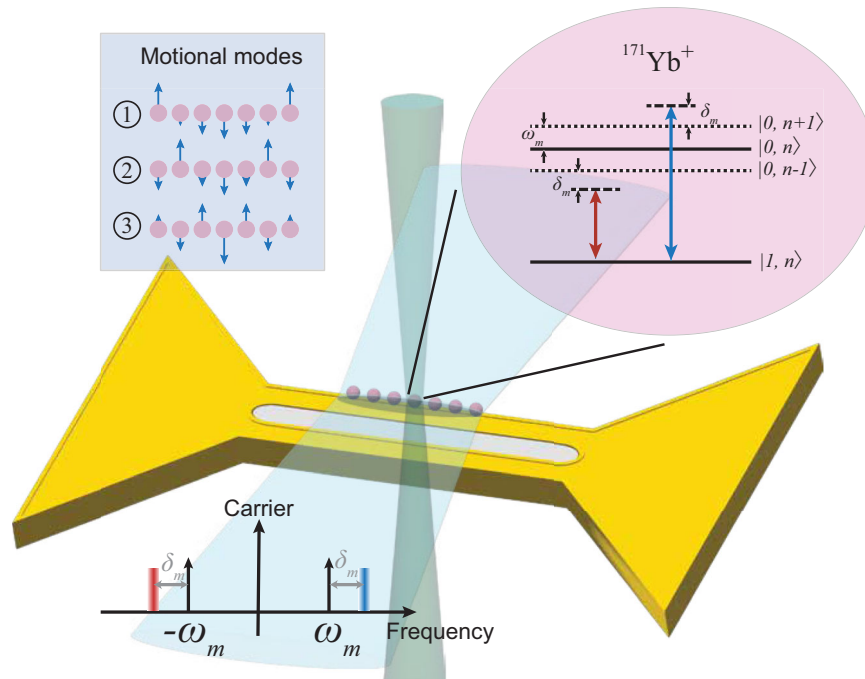


Fig. 1 | Schematic of the experimental setup. The ions are confined in a micro-fabricated surface trap. The spin states are encoded as the hyperfine clock states (qubit states) and the bosonic bath modes are encoded as the collective radial motional modes of the ion chain. We strategically use the center ion and the three symmetric modes (except for the center-of-mass mode, as shown in the upper left corner) in the experiment to minimize cross-mode couplings (see Methods). The

laser frequencies for the SDK operations are determined by the frequency difference between the two Raman beams, and are depicted by the red and blue lines on the frequency axis detuned by δ_m from the mode frequency ω_m , with the color gradients indicating the random frequencies used to implement the decoherence simulation.

the values $\bar{n}_0 = 0.036$ and $\Gamma = 0.0022\Delta$ are extracted from independent measurements characterizing imperfect cooling and finite motional coherence time, respectively. The experimentally measured revival amplitude (Fig. 2c) and fitted \bar{n} (Fig. 2d) match well with the predictions of noise-aware models. This shows that well-characterized experimental noise can serve as the baseline values for the thermal excitation and dephasing rate in the open quantum system model, and thus is not always a bottleneck for the accuracy of our simulations.

Next, we show the tunability of the dephasing rate Γ , which corresponds to the linewidth of the spin-boson model's spectral density. Dephasing is implemented by adding random frequency offsets to the SDK operations that simulate the time evolution (see Methods). This mimics the random fluctuations of the motional-mode frequency, following the stochastic model of motional dephasing noise in trapped-ion systems³⁶.

Figure 2b illustrates the dynamics for various values of Γ between 0 and 0.4Δ , which exhibit a crossover from underdamped to overdamped dynamics as Γ is increased (critical damping condition at $\Gamma \approx 0.18\Delta$). As the damping is increased beyond the critical point, the beat-note that signifies the excitation transfer from the spin to boson back to spin is suppressed, and there is a monotonic decrease in the oscillation of the donor population in the overdamped regime. We notice a π phase flip in the oscillation of the donor population in the beat-note in the underdamped case, signified by the phase difference between the underdamped and overdamped cases at $t \approx 2\pi/\Delta \times 10$.

The uncertainty of \bar{n} and Γ realized in the experiment can be reduced by performing a larger number of random trials, each trial using a different set of random parameters. The shaded areas in Fig. 2d and e show the standard deviation of fitted values for \bar{n} and Γ , obtained by numerical simulation of results averaged over 20 (pink) or 200 (blue) random trials. Our experiments are limited to 20 random trials due to the compiling delay required for each set of control parameters, and each trial is repeated 100 times to obtain the expectation value for

the donor population. The experimental data is consistent with the standard deviation derived from 20 numerical trials. We expect to readily increase the number of random trials with fewer repetitions each in future experiments with faster compilation tools⁴⁰.

Engineering bath spectral densities

We can use multiple oscillator modes to engineer a target spectral density structure for the oscillator bath. We simulate a bath of spectral density composed of up to 3 Lorentzian peaks, each represented by a motional mode of the ion chain. The bath spectral density $J(\omega)$ in Fig. 3a is simulated using the SDK operations over two or three motional modes. Figure 3b shows the frequencies of the laser pulses used to drive the SDK, defined as the detuning of laser beams from the carrier transition frequency. The 1st, 3rd, and 5th motional modes are used, and the detuning of the laser frequency from each motional mode determines the frequency at which the bath spectral density is considered in Fig. 3a. We set the electronic coupling strength $\Delta = 500 \text{ cm}^{-141}$, such that at temperature 77 K, $\bar{n} \approx 0.1$ for the near-resonance vibrational modes. Figure 3c shows the results for simulating the dynamics of spin-boson models with spectral densities composed of 2 and 3 Lorentzian peaks, respectively. The theoretical predictions are obtained using the time-dependent density-matrix renormalization group algorithm in the interaction picture⁴². The donor population features underdamped coherent oscillations, with contributions from all three modes. The measured population closely follows the theoretical predictions.

The coherence time of the motional modes in our setup of $\sim 5.2(7) \text{ ms}$ is the leading source of noise^{36,43}, and is comparable to the experimental time for simulating the time evolution under spectral densities generated from 2 mode (1.63 ms) and 3-mode (2.56 ms) cases. For these simulations, the contribution of motional decoherence in the experiment is identical to the random kicks that we apply in the spin-oscillator model to simulate the bath, and can be

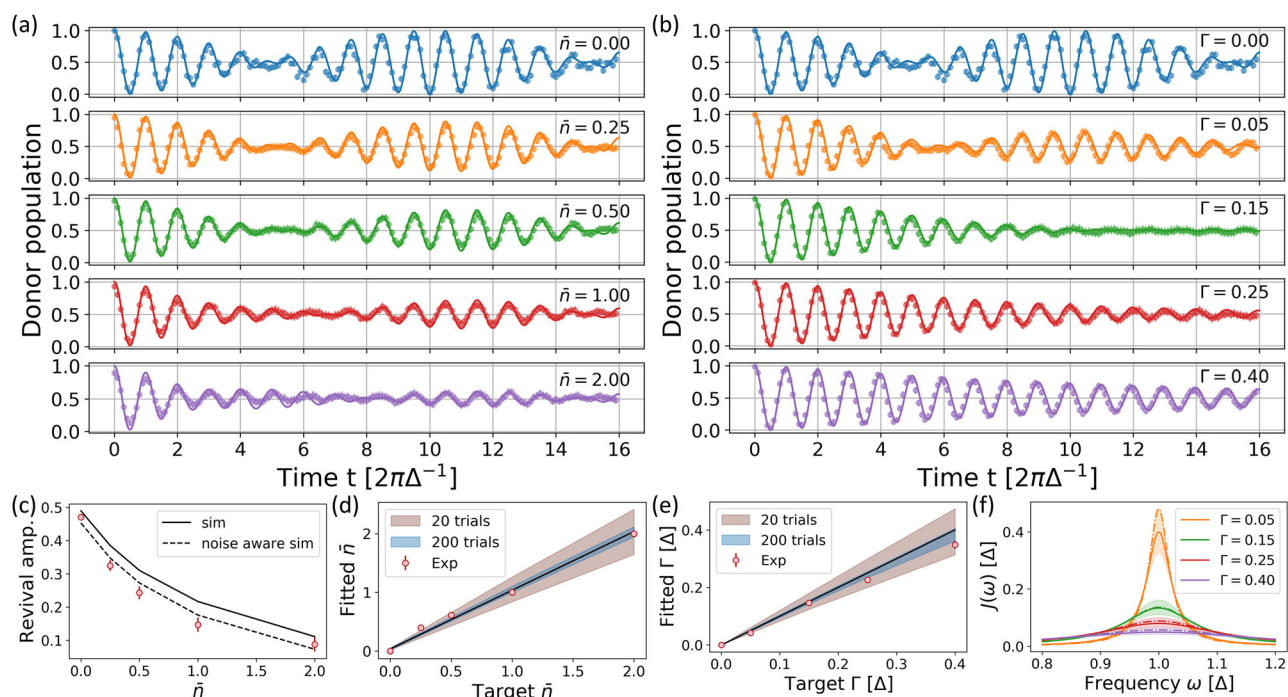


Fig. 2 | Demonstration of the tunability of the bath's initial temperature and spectral linewidth. **a** Dynamics of the coherent spin-single oscillator model \hat{H}_D with various values of average phonon number \bar{n} for the oscillator's initial state. **b** Dynamics of the model with $\bar{n} = 0$, $J(\omega) = J_{L_0}(\omega)$ (single peak) and various values of $\Gamma_1 = \Gamma$. For both **(a)** and **(b)**, $\epsilon = 0$, $\nu_1 = \Delta$, and $\kappa_1 = 0.1\Delta$. Lines and dots represent theoretical predictions and experimental data, respectively. The error bars (size comparable to the symbols in these two plots) denote measured standard deviation over 20 trials, each trial performed with randomly drawn set of parameters and repeated 100 times. **c** Revival amplitude versus \bar{n} . Predictions of the original (solid line) model and the noise-aware (dashed line) model are compared with the

experimental results (circles). **d** Measured values of \bar{n} fitted to the predictions of the noise-aware model. The solid line depicts $y = x + \bar{n}_0$, where $\bar{n}_0 = 0.036$ is the expected offset in the phonon number due to imperfect cooling. **e** Measured values of Γ fitted to the theoretical predictions with $\bar{n} = \bar{n}_0$. The solid line depicts $y = x$. In **(d)** and **(e)**, the blue and brown shaded regions represent the expected uncertainty of the value when the populations are averaged over 20 and 200 random trials, respectively. **f** Lorentzian spectral densities for various target (solid) and fitted (dashed) values of Γ . The shaded region represents the expected uncertainty of Γ when averaged over 20 random trials.

incorporated as the source of dephasing in our simulation with proper calibration⁴³.

Leggett spin-boson models

We further simulate the spin-boson models inspired by Leggett et al.¹. The spectral density of the bath is given by

$$J_{\text{Legg}}(\omega) = A\omega^s \omega_c^{1-s} e^{-\omega/\omega_c}, \quad (4)$$

where ω_c is the cutoff frequency, and $s < 1$, $s = 1$, and $s > 1$ represent the sub-Ohmic, Ohmic, and super-Ohmic baths, respectively. This model is widely used to characterize the noise in nanomechanical devices⁴⁴, superconducting circuits^{12,45}, and proton-transfer reactions^{46,47}. The spin dynamics exhibit various behaviors, such as coherent oscillations, incoherent decay, and localization, depending on the values of s and A , which has been a subject of longstanding research using analytical tools^{1,48} and classical simulations^{29–31,49}.

Recognizing that the spin exchanges energy with the bath only near its resonance, we use a sum of Lorentzian lines from motional modes to approximate the spectral density $J_{\text{Legg}}(\omega)$ near the resonance frequency Δ , with the cutoff frequency set to be much higher ($\omega_c = 10\Delta$). We utilize well-established global optimization algorithms to find the optimal set of parameters (κ_l , Γ_l , and ν_l in Eq. (3)) that best represent $J_{\text{Legg}}(\omega)$ (see Section V of the Supplementary Material). Using this approach, we consider weak spin-bath coupling ($A = 0.1$) and match the spectral density within the target bandwidth $\omega \in [0.9\Delta, 1.1\Delta]$ with 2 Lorentzian peaks. Figure 4a shows the obtained spectra from the modes (solid lines) that approximate the spectral densities (dot-dashed lines) with $s = 0.5, 1.0$, and 2.0 , respectively. The results for the

donor population dynamics interacting with a bath featuring these approximated spectral densities are shown in Fig. 4b–d. We observe a crossover from near-coherent ($s = 2$) to fully damped ($s = 0.5$) oscillations in the simulated time scale, owing to the different levels of spectral density $J(\omega = \Delta)$ near resonance. The experimental data match well with theoretical predictions, where the deviations in Fig. 4d result from an insufficient number of Trotterization steps (Supplementary Fig. 5). Simulations of baths with fixed $J(\omega = \Delta)$ value over varying levels of the s parameter (ranging from $s = 0.3$ to $s = 3$) are shown in Section VI of the Supplementary Material (Supplementary Fig. 6).

Vibration-assisted energy transfer

Finally, we simulate the VAET model²⁴ with nonzero energy detuning ϵ between the spin states. Here we set the spin parameters as $\Delta = 30\text{cm}^{-1}$ and $\epsilon = 100\text{cm}^{-1}$. In the absence of coupling to a vibrational mode ($\kappa = 0\text{cm}^{-1}$), energy transfer between the detuned spin states is suppressed; however, for nonzero κ , the energy transfer can be activated if the mode frequency ν meets the resonance condition (single mode's index $l = 1$ omitted).

Figure 5a shows the experimental data for simulating the coherent spin-single oscillator model \hat{H}_D with a relatively large coupling strength ($\kappa = 30\text{cm}^{-1}$). When ν satisfies the resonance condition of VAET ($\nu = \sqrt{\Delta^2 + \epsilon^2}/k \approx 104\text{cm}^{-1}/k$ where k is an integer), energy transfer occurs²⁴. Otherwise, energy remains localized at the donor state. Figure 5b shows the impact of initial temperature of the oscillator on the resonant VAET ($\nu = 104\text{cm}^{-1}$). We create baths of two temperatures 0 K and 300 K corresponding to initial average phonon number $\bar{n} = 0$ and 2.0 , respectively. The energy transfer is faster for higher \bar{n} in the beginning as more vibrational quanta assist the energy

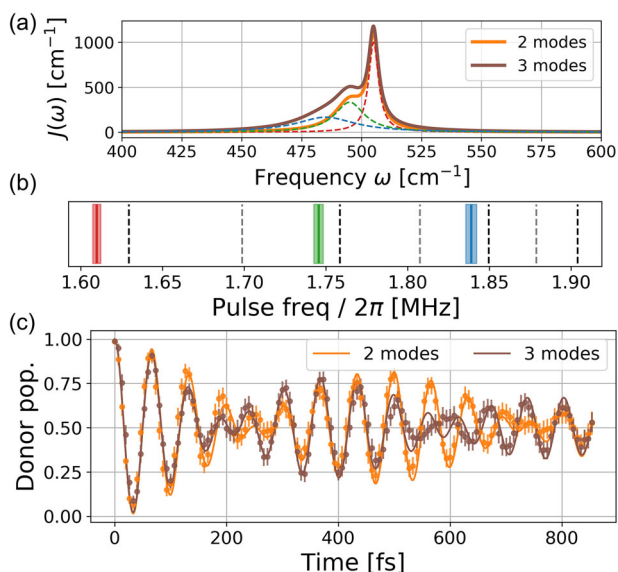


Fig. 3 | Simulations of molecular energy transfer in model structured baths. **a** Simulated spectral density of the spin-boson model's bath, where the electronic coupling strength $\Delta = 500\text{cm}^{-1}$. The orange and brown solid curves illustrate the spectral densities summed over two and three peaks, respectively. **b** Dashed lines represent the radial motional modes that are coupled by the Raman beam. Black or grey dashed lines represent modes with non-zero or zero coupling strength to the target ion, respectively. The three solid lines and the shaded regions depict the mean value and the standard deviation of the randomized pulse frequencies, and the color corresponds to the Lorentzian peak generating the final spectral density in **(a)**. **c** Time evolution of the spin-boson models with $J(\omega)$ in **(a)**. The x-axis represents the simulated time of the chemical model, determined by the chosen model parameters (see Section I of the Supplementary Material). The bath temperature is 77 K such that $\bar{n} \approx 0.1$, which is set for trapped ions' motional modes using imperfect sideband cooling. Curves and dots represent theoretical predictions and experimental data, respectively. Error bars are derived as in Fig. 2.

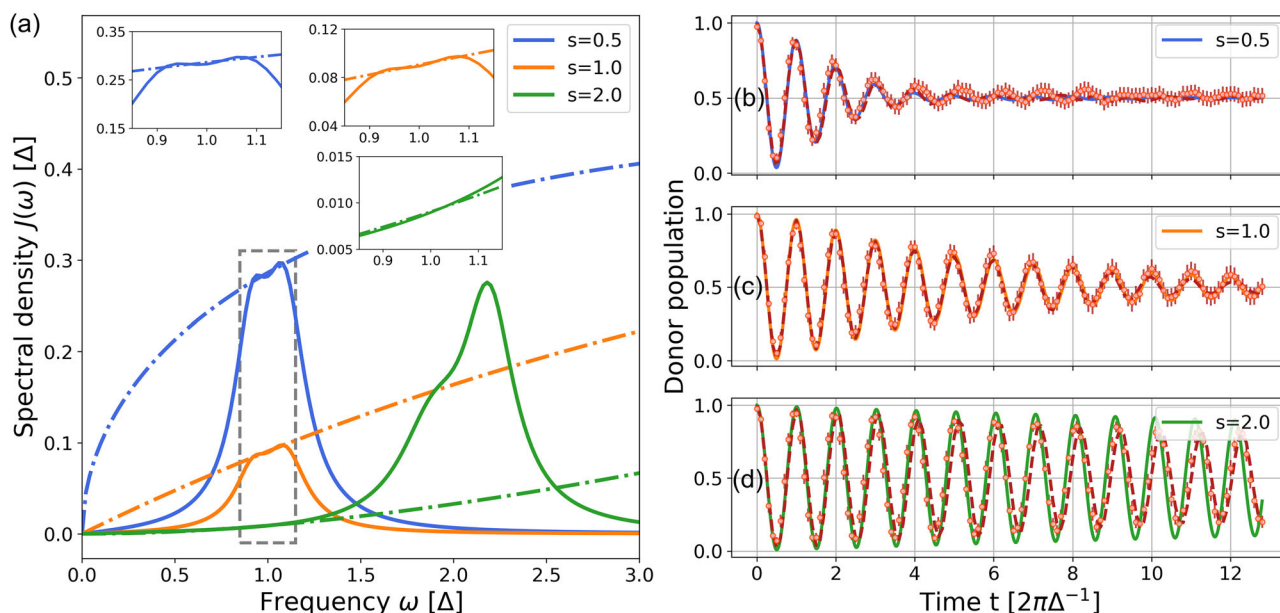


Fig. 4 | Simulations based on Leggett's spin-boson model. **a** Spectral densities of the Leggett's model. Dot-dashed curves are the sub-Ohmic ($s = 0.5$), Ohmic ($s = 1.0$), and super-Ohmic ($s = 2.0$) spectral densities described by Eq. (4) ($A = 0.1$, $\omega_c = 10\Delta$). Solid curves are the spectral densities simulated in our experiments using two motional modes. These spectral densities are designed to match the dot-dashed curves near $\omega = \Delta$. Insets compare the solid and dot-dashed curves within the interval $\omega \in [0.85\Delta, 1.15\Delta]$. **(b)(c)(d)** Dynamics of the spin-boson model for $s = 0.5, 1.0$, and

transfer, but it also leads to a rapid decay of oscillations over time as the coherence is lost.

In Fig. 5c, we simulate the dephased spin-oscillator model with $\Gamma = 10\text{cm}^{-1}$ and various values of κ , to study the impact of dissipative coupling. We note that in the weak- κ regime (or short evolution time), the results agree with the theoretical predictions of the damped spin-oscillator model, which is equivalent to those of the spin-boson model with $J(\omega) = J_{Lo}(\omega)^{15,32}$; however, as κ is increased, the dephased and damped models' dynamics deviate. This is expected because, unlike the damped model, the dephased model does not extract energy from the spin-oscillator system, so the donor population will not decay towards zero even after a long time evolution when coupled to a single-oscillator bath. This example demonstrates that our method provides the ability to simulate a wider range of dissipative channels in the study of open system dynamics.

Discussion

While classical simulation approaches to open dissipative systems continue to improve with advancements in numerical methods, they encounter fundamental challenges when dealing with large quantum systems that span exponentially large Hilbert space^{17,18}. Take, for example, the Dissipation-Assisted Matrix Product Factorization (DAMPF) method, a state-of-the-art method for simulating open quantum systems⁵⁰. For simulating a one-dimensional chain of N_s electronic states, each coupled to a bath of N_b damped bosonic modes, the computational complexity of DAMPF scales as $\mathcal{O}(N_s^5 N_b D_b^2 \chi^3)$, where D_b is the number of energy levels that represent each bosonic mode and χ is the bond dimension in the matrix product operator representation of the system-bath density matrix. A critical issue is the rapid, potentially exponential increase in χ with respect to the system-bath coupling strength, for a fixed target accuracy in the population dynamics. For these types of problems, trapped-ion simulators may offer a more scalable alternative, as the number of operations scales only as $\mathcal{O}(N_s N_b)$ and the total duration of SDK operations grows linearly with the system-bath coupling strength¹⁸. The current state-of-the-

2.0, respectively. The solid curves represent the theoretical predictions of the spin-boson models with spectral densities given by the solid curves in **(a)**. The red dashed curves are expected results, derived from numerical simulations of the density matrix of the qubit and motional modes subject to control operations and hardware noise. Circles denote experimental data and error bars indicate the standard deviation over 60, 20, and 20 trials for **(b)**, **(c)**, and **(d)**, respectively (More trials were needed to overcome the shot noise in **(b)** when the donor population is near 0.5).

art trapped-ion systems offer several dozens of highly coherent spins and bosonic modes that are very densely coupled with each other, the complete quantum description of which is totally intractable with classical computers of today^{51–53}. Developing various control methods over these quantum systems to study important physical, chemical,

biological and material systems of critical interest will open up a new computational framework in science.

The methods developed in this work utilize fully programmable control methods to simulate dissipative processes. The dephased oscillator method can be used to realize non-Gaussian bath models⁵⁴, relevant for studying physical processes such as localization transitions in strongly-coupled spin-boson models^{1,29–31,49} and role of bosonic dephasing in molecular energy transfer^{55,56}. The capability to measure the probability distribution of the motional modes^{20–23} may further reveal the effects of intricate vibronic interactions in biological and chemical reaction dynamics. High accuracy simulations will require development of efficient characterization methods⁵⁷ and novel control protocols in the trapped-ion system⁵⁸ to implement various interaction terms in the target Hamiltonian. Combined with damped spin-boson models that can be implemented using sympathetic cooling³⁴, the long-chain trapped-ion systems can provide a versatile platform for simulating dynamics of complex open quantum systems.

The number of readily usable transverse boson modes scales as $2(N - 1)$ (two transversal directions, less the center-of-mass mode subject to external technical noise), and the coupling strength of each ion to each mode is given by the mode participation factor (relative displacement of each ion when the mode is excited). In future experiments on longer ion chains involving operations on a larger number of modes, the mode spacing must be maintained to reduce cross-mode coupling which can be achieved by tightening the longitudinal confinement at the expense of smaller ion spacing. Further reduction of the cross-mode coupling can be achieved by reducing the laser power, at the expense of slowing down the simulation dynamics. Alternatively, the SDK control pulses can be designed to actively suppress cross-mode coupling¹⁸ (see Section VII of the Supplementary Material for details). The properties of the phonon states cannot be measured directly, and characterization of the boson modes requires mapping of boson properties to ion qubits that require many repetitions^{19–21}. Novel and efficient methods to characterize the boson modes or spin-boson correlations are highly desired.

Methods

Experimental implementation of SDK operations

The experiments are performed using a linear chain of $^{171}\text{Yb}^+$ ions. We use the hyperfine energy levels $|0\rangle \equiv |F=1; m_f=0\rangle$ and $|1\rangle \equiv |F=0; m_f=0\rangle$ in the $^2S_{1/2}$ manifold as the qubit states (spin states). The collective radial motional modes of the ion chain are used to represent the bosonic bath modes (see Fig. 6a).

Through the sequential application of Doppler cooling, EIT cooling, and sideband cooling, the zig-zag motional mode of the 7-ion

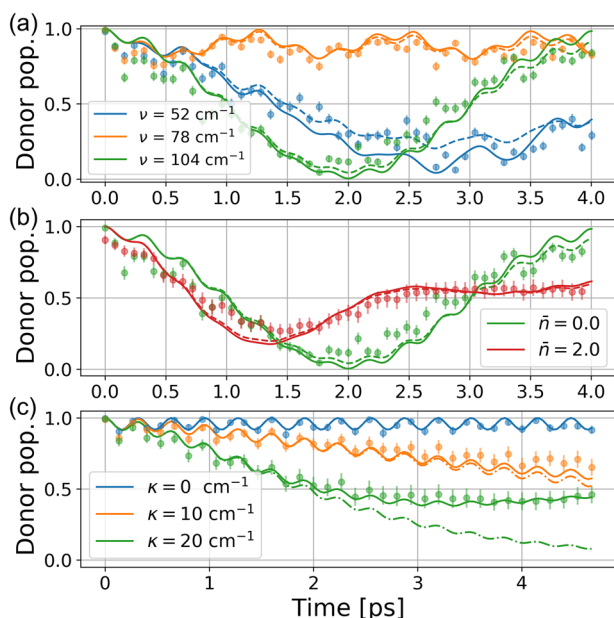


Fig. 5 | Simulations of vibration-assisted energy transfer (VAET). We set $\epsilon = 100 \text{ cm}^{-1}$ and $\Delta = 30 \text{ cm}^{-1}$. The x-axis represents the simulated time of the chemical model, determined by the chosen model parameters (see Section I of the Supplementary Material). **a, b** Time evolution of the donor-state population for coherent VAET models with $\kappa = 30 \text{ cm}^{-1}$. Solid and dashed curves depict theoretical predictions of the ideal target and the noise-aware model, respectively. Circles represent experimental data and error bars are the standard deviation over 100 repetitions. In **(a)**, bath temperature is fixed at 0 K ($\bar{n}=0$) and ν is varied. In **(b)**, ν is fixed to the resonant value 104 cm^{-1} and two temperatures 0 K and 300 K, which correspond to $\bar{n}=0$ and 2.0, respectively, are simulated. **c** Time evolution of the donor-state population for dissipative VAET models with $\nu = 104 \text{ cm}^{-1}$ and $\Gamma = 10 \text{ cm}^{-1}$ at 0 K. Solid and dot-dashed curves depict theoretical predictions of the dephased spin-oscillator model and the damped spin-oscillator model, respectively. Circles denote experimental data. For $\kappa = 0 \text{ cm}^{-1}$, error bars indicate the standard deviation over 100 repetitions. For $\kappa = 10$ and 20 cm^{-1} , error bars indicate the standard deviation over 20 trials, each trial performed with a randomly drawn set of parameters and repeated 100 times.

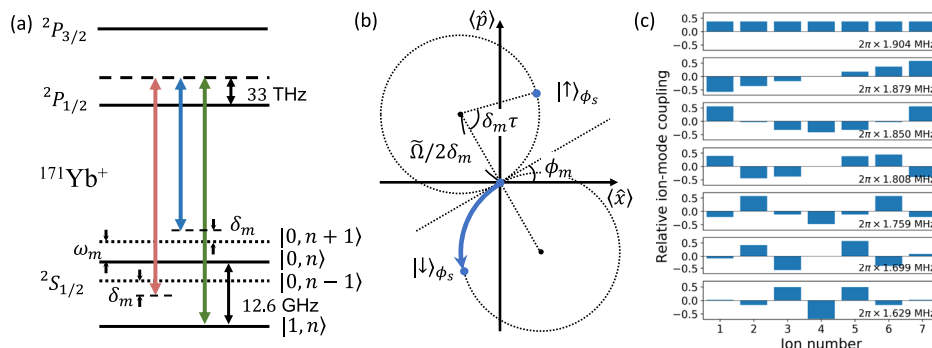


Fig. 6 | SDK operation and motional-mode structure. **a** Simplified energy levels of the $^{171}\text{Yb}^+$ ion and the laser pulses used for implementing the on-resonance spin-dependent kick (SDK) operation. The global beam consists of two tones driving the blue sideband (BSB) and red sideband (RSB) transitions, accompanied by the individual beam (green arrow), respectively. **b** Visualization of the motional-state evolution in phase space when a SDK operation of duration τ is applied, where the

qubit is in the eigenstate of the operator $\hat{\sigma}_{\phi_s} \equiv \hat{\sigma}_+ e^{i\phi_s} + \hat{\sigma}_- e^{-i\phi_s}$. Here, $\hat{\sigma}_+$ ($\hat{\sigma}_-$) is the raising (lowering) operator of the qubit, ϕ_s (ϕ_m) is the spin (motion) phase of the laser beams, $\tilde{\Omega}$ is the Rabi frequency of the sideband transition, and δ_m is the motion detuning. **c** Normalized eigenvector components of each motional mode, which represent the relative ion-mode coupling strengths. Motional-mode frequencies are shown in the lower right corner of each panel.

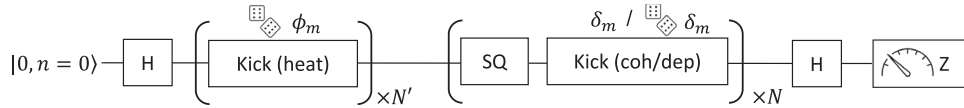


Fig. 7 | Instruction of operations for simulating the dephased spin-oscillator model. ‘H’ represents the Hadamard gate on the qubit. ‘Kick (heat)’ represents the SDK operations with random ϕ_m that prepare the thermal state on average. ‘SQ’ and ‘Kick (coh/dep)’ represent the single-qubit rotations and SDK

operations that simulate the first and second terms in Eq. (5), respectively. Coherent or dephased spin-oscillator model is simulated by using a fixed or randomly drawn δ_m value at each step, respectively.

chain can be cooled to average phonon number $\bar{n} = 0.036(16)$. Following this, a 370 nm laser is utilized to pump the ions to their ground state $|1\rangle$. Transitions between the qubit states are performed using stimulated Raman transitions driven by a pair of laser beams³⁶. Acousto-optic modulators are employed to manipulate the frequency and phase of each laser beam, thereby enabling single-qubit gates; we apply a bit flip (X) gate to initialize the ion to the $|0\rangle$ state. The spin-oscillator coupling is simulated using the spin-dependent kick (SDK) operation induced by simultaneous blue- and red-sideband transitions as shown in Fig. 1. Figure 6b visualizes how the motional state evolves in phase space when a SDK operation of duration τ , spin (motion) phase ϕ_s (ϕ_m), motion detuning δ_m , and sideband Rabi frequency $\tilde{\Omega}$ is applied⁵⁹. High fidelity SDK operation requires careful calibration of the light shift (Supplementary Fig. 1) and the motional frequency (Supplementary Fig. 2). Subsequent to the final operation, the qubit-state population is accessed via the state-dependent detection technique.

The Lamb-Dicke parameters of the 7 motional modes range from 0.073 to 0.079 due to their different frequencies. The relative ion-mode coupling strengths (normalized eigenvector components) are shown in Fig. 6c. We strategically use the center ion of a 7-ion chain, as it exhibits negligible coupling to the 2nd, 4th, and 6th modes. This arrangement maximizes the effective spacing between the motional-mode frequencies and therefore suppresses cross-mode coupling (driving modes that are not targeted by the SDK operation).

Trotterization

The evolution of \hat{H}_D in Eq. (2) is mapped to a sequence of single-qubit rotations and SDK operations via Trotterization. After conjugating \hat{H}_D with a Hadamard gate on the qubit, the Hamiltonian can be described in the interaction picture as

$$\hat{H}_I(t) = \frac{\epsilon}{2} \hat{\sigma}_\Delta(t) + \frac{\kappa}{2} \hat{\sigma}_\Delta(t) (\hat{b} e^{-i\nu t} + \hat{b}^\dagger e^{i\nu t}), \tag{5}$$

where $\hat{\sigma}_\Delta(t) \equiv \hat{\sigma}_+ e^{i\Delta t} + \hat{\sigma}_- e^{-i\Delta t}$ and $\hat{\sigma}_+$ ($\hat{\sigma}_-$) is the raising (lowering) operator of the qubit. The evolution with respect to $\hat{H}_I(t)$ is discretized into N time steps, each consisting of a single-qubit rotation and an SDK operation that simulates the first and second term, respectively. Specifically, for the SDK operation at the j -th time step, the spin (motion) phase of the laser beams⁵⁹ is set as Δt_j (νt_j), where $t_j \equiv (j - \frac{1}{2})T/N\tau$ and τ is the duration of the operation for each time step. This is equivalent to setting the symmetric (anti-symmetric) detuning from the sideband transitions, referred to as the spin (motion) detuning, as $\Delta T/N\tau$ ($\nu T/N\tau$) at all time steps. This method can be straightforwardly extended to simulating models with multiple electronic states and vibrational modes^{18,37}; however, the laser phase needs to be tuned to track the phase of each motional mode correctly (Supplementary Fig. 3 in Section II of the Supplementary Material).

Randomized operations

Randomizing the control parameters is a key ingredient in our approach to simulating dissipation mechanisms in spin-boson models. By taking an average of many coherent evolutions, each involving a stochastically varying parameter, we realize both heating and

dephasing as described by the Lindblad master equation³⁸. Heating and dephasing are used to tune the initial temperature and spectral linewidth of the bath, respectively.

First, the bosonic mode at finite temperature is created by modeling the mode’s heating process as interacting with an infinite-temperature external bath for a finite duration. This heating is described by a pair of Lindblad operators $\hat{L}_1 = \sqrt{\Gamma} \hat{b}$ and $\hat{L}_2 = \sqrt{\Gamma} \hat{b}^\dagger$, where Γ is the heating rate. We first prepare the motional mode at the ground state, and then apply N' resonant ($\delta_m = 0$) SDK operations of duration $\tau' = 4\Gamma/\tilde{\Omega}^2$, spin phase $\phi_s = 0$, and motion phase ϕ_m randomly drawn from $[0, 2\pi)$ for each operation. These stochastic operations are applied on the initial qubit-mode composite state $|+, n=0\rangle$; note that $|+\rangle$ is an eigenstate of the spin operator with $\phi_s = 0$, and thus the qubit is decoupled from these operations. When averaged over many trials of coherent evolutions, each executed with a distinct set of N' random ϕ_m values, this procedure prepares the thermal state with an average phonon number $\bar{n} = N\Gamma\tau'$ (derivation provided in Section IV of the Supplementary Material). This can be intuitively understood as the thermal state represented as an ensemble of randomly displaced coherent states. For the experimental data in Fig. 2a and Fig. 5b, the average phonon number \bar{n} of the initial thermal state is tuned by varying the duration τ' of SDK operations, where the number of steps N' is fixed to 5. The errors in \bar{n} due to finite number of steps are discussed in Section IV of the Supplementary Material.

Next, dephasing during the time evolution, which is described by a single Lindblad operator $\hat{L}_1 = \sqrt{\Gamma} \hat{b}^\dagger \hat{b}$, is induced by giving random offsets to the motion detuning δ_m of the N Trotterized SDK operations. Specifically, an offset to δ_m is assigned for each of the N steps, with values drawn from a normal distribution characterized by a mean of zero and a standard deviation of $\sqrt{\Gamma T/N}/\tau$ (see Section IV of the Supplementary Material). The qubit population dynamics averaged over many trials of coherent evolutions, each performed with a set of N random δ_m values, give the dynamics with respect to the dephased spin-oscillator model. The entire instruction of operations is shown in Fig. 7.

In practice, the dephasing strength Γ is varied by tuning the standard deviation of the random offsets to δ_m at each Trotterization step. This enables tuning the FWHM of each Lorentzian peak in the bath’s spectral density. The errors in the simulated dephasing strength due to a finite number of Trotterization steps are discussed in Section IV of the Supplementary Material (Supplementary Fig. 5).

Data availability

Source data for all main text figures are available in ref. 60. Any other data supporting the findings of this study are available upon request.

Code availability

The code used for the simulation and analysis of the data is available upon request.

References

1. Leggett, A. J. et al. Dynamics of the dissipative two-state system. *Rev. Mod. Phys.* **59**, 1–85 (1987).
2. Caldeira, A. O. & Leggett, A. J. Quantum tunnelling in a dissipative system. *Ann. Phys.* **149**, 374–456 (1983).

3. Weiss, U., Grabert, H. & Linkwitz, S. Influence of friction and temperature on coherent quantum tunneling. *J. Low. Temp. Phys.* **68**, 213–244 (1987).
4. Garg, A., Onuchic, J. N. & Ambegaokar, V. Effect of friction on electron transfer in biomolecules. *J. Chem. Phys.* **83**, 4491–4503 (1985).
5. Gilmore, J. & McKenzie, R. H. Spin boson models for quantum decoherence of electronic excitations of biomolecules and quantum dots in a solvent. *J. Phys. Condens. Matter* **17**, 1735 (2005).
6. Strack, P. & Sachdev, S. Dicke quantum spin glass of atoms and photons. *Phys. Rev. Lett.* **107**, 277202 (2011).
7. Bhaseen, M. J., Mayoh, J., Simons, B. D. & Keeling, J. Dynamics of nonequilibrium dicke models. *Phys. Rev. A* **85**, 013817 (2012).
8. Huelga, S. F. & Plenio, M. B. Vibrations, quanta and biology. *Contemp. Phys.* **54**, 181–207 (2013).
9. Jang, S. J. & Mennucci, B. Delocalized excitons in natural light-harvesting complexes. *Rev. Mod. Phys.* **90**, 035003 (2018).
10. Mostame, S. et al. Quantum simulator of an open quantum system using superconducting qubits: exciton transport in photosynthetic complexes. *N. J. Phys.* **14**, 105013 (2012).
11. Leppäkangas, J. et al. Quantum simulation of the spin-boson model with a microwave circuit. *Phys. Rev. A* **97**, 052321 (2018).
12. Magazzù, L. et al. Probing the strongly driven spin-boson model in a superconducting quantum circuit. *Nat. Commun.* **9**, 1403 (2018).
13. Kim, C. W., Nichol, J. M., Jordan, A. N. & Franco, I. Analog quantum simulation of the dynamics of open quantum systems with quantum dots and microelectronic circuits. *PRX Quantum* **3**, 040308 (2022).
14. Porras, D., Marquardt, F., Delft, J. & Cirac, J. I. Mesoscopic spin-boson models of trapped ions. *Phys. Rev. A* **78**, 010101 (2008).
15. Lemmer, A. et al. A trapped-ion simulator for spin-boson models with structured environments. *N. J. Phys.* **20**, 073002 (2018).
16. Schlawin, F., Gessner, M., Buchleitner, A., Schätz, T. & Skourtis, S. S. Continuously parametrized quantum simulation of molecular electron-transfer reactions. *PRX Quantum* **2**, 010314 (2021).
17. MacDonell, R. J. et al. Analog quantum simulation of chemical dynamics. *Chem. Sci.* **12**, 9794–9805 (2021).
18. Kang, M. et al. Seeking a quantum advantage with trapped-ion quantum simulations of condensed-phase chemical dynamics. *Nat. Rev. Chem.* **8**, 340–358 (2024).
19. Chen, W. et al. Scalable and programmable phononic network with trapped ions. *Nat. Phys.* **19**, 877–883 (2023).
20. Flühmann, C. & Home, J. P. Direct characteristic-function tomography of quantum states of the trapped-ion motional oscillator. *Phys. Rev. Lett.* **125**, 043602 (2020).
21. Jia, Z. et al. Determination of multimode motional quantum states in a trapped ion system. *Phys. Rev. Lett.* **129**, 103602 (2022).
22. Whitlow, J. et al. Quantum simulation of conical intersections using trapped ions. *Nat. Chem.* **15**, 1509–1514 (2023).
23. Valahu, C. H. et al. Direct observation of geometric-phase interference in dynamics around a conical intersection. *Nat. Chem.* **15**, 1503–1508 (2023).
24. Gorman, D. J. et al. Engineering vibrationally assisted energy transfer in a trapped-ion quantum simulator. *Phys. Rev. X* **8**, 011038 (2018).
25. MacDonell, R. J. et al. Predicting molecular vibronic spectra using time-domain analog quantum simulation. *Chem. Sci.* **14**, 9439–9451 (2023).
26. Wang, G.-X. et al. Simulating the spin-boson model with a controllable reservoir in an ion trap. *Phys. Rev. A* **109**, 062402 (2024).
27. Lee, M. K. & Coker, D. F. Modeling electronic-nuclear interactions for excitation energy transfer processes in light-harvesting complexes. *J. Phys. Chem. Lett.* **7**, 3171–3178 (2016).
28. Kim, C. W., Choi, B. & Rhee, Y. M. Excited state energy fluctuations in the Fenna–Matthews–Olson complex from molecular dynamics simulations with interpolated chromophore potentials. *Phys. Chem. Chem. Phys.* **20**, 3310–3319 (2018).
29. Wang, H. & Thoss, M. From coherent motion to localization: dynamics of the spin-boson model at zero temperature. *N. J. Phys.* **10**, 115005 (2008).
30. Duan, C., Tang, Z., Cao, J. & Wu, J. Zero-temperature localization in a sub-Ohmic spin-boson model investigated by an extended hierarchy equation of motion. *Phys. Rev. B* **95**, 214308 (2017).
31. Strathearn, A., Kirton, P., Kilda, D., Keeling, J. & Lovett, B. W. Efficient non-Markovian quantum dynamics using time-evolving matrix product operators. *Nat. Commun.* **9**, 3322 (2018).
32. Tamascelli, D., Smirne, A., Huelga, S. F. & Plenio, M. B. Non-perturbative treatment of non-Markovian dynamics of open quantum systems. *Phys. Rev. Lett.* **120**, 030402 (2018).
33. Allcock, D. et al. *omg* blueprint for trapped ion quantum computing with metastable states. *Appl. Phys. Lett.* **119**, 214002 (2021).
34. So, V. et al. Trapped-ion quantum simulation of electron transfer models with tunable dissipation. *Sci. Adv.* **10**, 8011 (2024).
35. Revelle, M.C.: Phoenix and peregrine ion traps. arXiv:2009.02398 (2020).
36. Wang, Y. et al. High-fidelity two-qubit gates using a microelectromechanical-system-based beam steering system for individual qubit addressing. *Phys. Rev. Lett.* **125**, 150505 (2020).
37. Sun, K. et al. Quantum simulation of polarized light-induced electron transfer with a trapped-ion qutrit system. *J. Phys. Chem. Lett.* **14**, 6071–6077 (2023).
38. Chenu, A., Beau, M., Cao, J. & Campo, A. Quantum simulation of generic many-body open system dynamics using classical noise. *Phys. Rev. Lett.* **118**, 140403 (2017).
39. Eberly, J. H., Narozhny, N. & Sanchez-Mondragon, J. Periodic spontaneous collapse and revival in a simple quantum model. *Phys. Rev. Lett.* **44**, 1323 (1980).
40. Dalvi, A.S. et al. One-time compilation of device-level instructions for quantum subroutines. In: 2024 IEEE International Conference on Quantum Computing and Engineering (QCE), vol. 1, pp. 873–884 (2024).
41. Chenu, A. & Scholes, G. D. Coherence in energy transfer and photosynthesis. *Annu. Rev. Phys. Chem.* **66**, 69–96 (2015).
42. Nuomin, H., Beratan, D. N. & Zhang, P. Improving the efficiency of open-quantum-system simulations using matrix product states in the interaction picture. *Phys. Rev. A* **105**, 032406 (2022).
43. Kang, M. et al. Designing filter functions of frequency-modulated pulses for high-fidelity two-qubit gates in ion chains. *Phys. Rev. Appl.* **19**, 014014 (2023).
44. Galland, C., Högele, A., Türeci, H. E. & Imamoğlu, A. Non-Markovian decoherence of localized nanotube excitons by acoustic phonons. *Phys. Rev. Lett.* **101**, 067402 (2008).
45. Kaur, K. et al. Spin-boson quantum phase transition in multilevel superconducting qubits. *Phys. Rev. Lett.* **127**, 237702 (2021).
46. Ohta, Y., Soudackov, A. V. & Hammes-Schiffer, S. Extended spin-boson model for nonadiabatic hydrogen tunneling in the condensed phase. *J. Chem. Phys.* **125**, 144522 (2006).
47. Craig, I. R., Thoss, M. & Wang, H. Proton transfer reactions in model condensed-phase environments: Accurate quantum dynamics using the multilayer multiconfiguration time-dependent Hartree approach. *J. Chem. Phys.* **127**, 144503 (2007).
48. Bulla, R., Tong, N.-H. & Vojta, M. Numerical renormalization group for bosonic systems and application to the sub-Ohmic spin-boson model. *Phys. Rev. Lett.* **91**, 170601 (2003).
49. Nalbach, P. & Thorwart, M. Crossover from coherent to incoherent quantum dynamics due to sub-ohmic dephasing. *Phys. Rev. B* **87**, 014116 (2013).
50. Somoza, A. D., Marty, O., Lim, J., Huelga, S. F. & Plenio, M. B. Dissipation-assisted matrix product factorization. *Phys. Rev. Lett.* **123**, 100502 (2019).

51. Cetina, M. et al. Control of transverse motion for quantum gates on individually addressed atomic qubits. *PRX Quantum* **3**, 010334 (2022).
52. Chen, J.-S. et al. Benchmarking a trapped-ion quantum computer with 30 qubits. *Quantum* **8**, 1516 (2024).
53. DeCross et al. The computational power of random quantum circuits in arbitrary geometries. Preprint at: [arXiv:2406.02501v3](https://arxiv.org/abs/2406.02501v3) (2024).
54. Barthel, T. & Zhang, Y. Solving quasi-free and quadratic Lindblad master equations for open fermionic and bosonic systems. *J. Stat. Mech.* **2022**, 113101 (2022).
55. Stock, G. & Domcke, W. Theory of resonance Raman scattering and fluorescence from strongly vibronically coupled excited states of polyatomic molecules. *J. Chem. Phys.* **93**, 5496–5509 (1990).
56. Banin, U., Bartana, A., Ruhman, S. & Kosloff, R. Impulsive excitation of coherent vibrational motion ground surface dynamics induced by intense short pulses. *J. Chem. Phys.* **101**, 8461–8481 (1994).
57. Kang, M., Liang, Q., Li, M. & Nam, Y. Efficient motional-mode characterization for high-fidelity trapped-ion quantum computing. *Quantum Sci. Technol.* **8**, 024002 (2023).
58. Lobser, D. et al. Jaqalpw: A guide to defining pulses and waveforms for Jaqal. Preprint at: [arXiv:2305.02311v1](https://arxiv.org/abs/2305.02311v1) (2023).
59. Lee, P. J. et al. Phase control of trapped ion quantum gates. *J. Opt. B Quantum Semiclass. Opt.* **7**, 371 (2005).
60. Sun, K. & Kang, M. Data from: Quantum simulation of spin-boson models with structured bath. <https://doi.org/10.7924/r42j6pj8s>.

Acknowledgements

The authors thank Yichao Yu for his valuable discussions about the phase tracking method, Daniel Lobser for his valuable suggestion in controlling the RFSoc control software, and Thomas Barthel for his course on open quantum systems that inspired this work. This research is funded by the Office of the Director of National Intelligence - Intelligence Advanced Research Projects Activity, through the ARO contract W911NF-16-1-0082 (provided the experimental apparatus used in the demonstration, K.R.B. and J.K.), the DOE BES award DE-SC0019400 (theoretical modeling, for K.R.B. and J.K.), and the NSF Quantum Leap Challenge Institute for Robust Quantum Simulation Grant No. OMA-2120757 (experimental concepts and validation, for K.S., M.K. and H.N.). Support is also acknowledged from the U.S. Department of Energy, Office of Science, National Quantum Information Science Research Centers, Quantum Systems Accelerator (data analysis and validation, for K.R.B. and J.K.).

Author contributions

K.S., M.K., K.R.B., and J.K. conceived the idea and developed a detailed methodology for experiments and modeling. K.S. and G.S. performed

the experiments, M.K., H.N., and D.N.B. performed modeling and simulations, K.S., M.K., K.R.B., and J.K. analyzed and validated the data. K.R.B. and J.K. supervised the project, K.S., M.K., and H.N. wrote the original draft, and K.S., M.K., and J.K. revised the manuscript. All authors discussed the results and reviewed the final manuscript.

Competing interests

J.K. and K.R.B. are shareholders of IonQ, Inc. The remaining authors declare no competing interests.

Additional information

Supplementary information The online version contains supplementary material available at <https://doi.org/10.1038/s41467-025-59296-y>.

Correspondence and requests for materials should be addressed to Jungsang Kim.

Peer review information *Nature Communications* thanks Patrick Becker and the other, anonymous, reviewer(s) for their contribution to the peer review of this work. A peer review file is available.

Reprints and permissions information is available at <http://www.nature.com/reprints>

Publisher's note Springer Nature remains neutral with regard to jurisdictional claims in published maps and institutional affiliations.

Open Access This article is licensed under a Creative Commons Attribution-NonCommercial-NoDerivatives 4.0 International License, which permits any non-commercial use, sharing, distribution and reproduction in any medium or format, as long as you give appropriate credit to the original author(s) and the source, provide a link to the Creative Commons licence, and indicate if you modified the licensed material. You do not have permission under this licence to share adapted material derived from this article or parts of it. The images or other third party material in this article are included in the article's Creative Commons licence, unless indicated otherwise in a credit line to the material. If material is not included in the article's Creative Commons licence and your intended use is not permitted by statutory regulation or exceeds the permitted use, you will need to obtain permission directly from the copyright holder. To view a copy of this licence, visit <http://creativecommons.org/licenses/by-nc-nd/4.0/>.

© The Author(s) 2025

